



Cite this: DOI: 10.1039/d0ce01403f

Crystal engineering construction of caffeic acid derivatives with potential applications in pharmaceuticals and degradable polymeric materials†

 Zhihan Wang,^a Quinton Flores,^a Hongye Guo,^b Raquel Trevizo,^a Xiaochan Zhang^a and Shihan Wang^c

Natural products are precious feedstock in drug discovery and sustainable materials. This work using crystal engineering strategy, visible light, and solvent-free cycloaddition successfully constructed two caffeic acid derivatives, *rel*-(1*R*,2*R*,3*S*,4*S*)-2,4-bis(3,4-dihydroxyphenyl)cyclobutane-1,3-dicarboxylate and *rel*-(1*R*,2*R*,3*S*,4*S*)-2,4-bis(3,4-dihydroxyphenyl)cyclobutane-1,3-dicarboxylic acid. Because of the multiple stereocenters, it is challenging to prepare those compounds using traditional organic synthesis methods. The crystal engineering Hirshfeld surface analysis and 2D intermolecular interaction fingerprints were applied to synthetic route design. The light resources used in this work was visible LED or free, clean, and renewable sunlight. The evidence suggested that pure stereoisomer was obtained demonstrating the stereospecificity and efficiency of the topochemical cycloaddition reaction. The derivatives exhibited free radical scavenging and antioxidant biological activities, as well as the potential inhibitory activity of fatty acid binding proteins. One of the derivatives is the precursor of the natural product shimobashiric acid C which paves the way for the total synthesis and further study of shimobashiric acid C. In addition, the derivatives possess photodegradability at a specific wavelength, which is very attractive for “green” degradable polymeric materials.

 Received 24th September 2020,
 Accepted 26th October 2020

DOI: 10.1039/d0ce01403f

rsc.li/crystengcomm

Introduction

Natural products play a crucial role in drug development and biomass-based materials.¹ Caffeic acid (CA) is a natural polyphenol and a key intermediate compound in lignin biosynthesis.² It is ubiquitous in the plant kingdom and can be extracted from many plants.² *In vitro* and *in vivo* studies have shown that CA and its derivatives possess variable biological activities, including antimicrobial, antiviral, antiinflammation, anticancer, antioxidants, antithrombosis, and antihypertensive activities.³ Especially, CA exhibited encouraging effects against a widespread cancer type

hepatocarcinoma.^{3d,4} One of the most studied caffeic acid derivatives is caffeic acid phenethyl ester (CAPE), which can be extracted from the popular propolis and is considered to be the main bioactive compound in propolis.⁵ According to previous reports, CAPE has a therapeutic effect on lung cancer, liver cancer, cholangiocarcinoma, and prostate cancer, and has been proven to inhibit colon cancer *in vivo*.^{3c,5,6} In addition, caffeic acid, as a secondary metabolite in plants, is the basis for the production of various plant metabolites.⁷ For example rosmarinic acid was first isolated and characterized from the *Rosmarinus officinalis* and has been found in a number of Lamiaceae plants.⁸ It was reported that rosmarinic acid has antioxidant and anti-inflammatory effects, inhibits the development of Alzheimer's disease, and is used in the treatment of asthma and allergic diseases.⁹ It can be synthesized by conventional organic synthesis methods using caffeic acid and salvianic acid A (danshensu) (Fig. 1a). Shimobashiric acid C, a dimer of rosmarinic acid, is also a derivative of caffeic acid which can be isolated from *Keiskea japonica* and *Plectranthus amboinicus*.¹⁰ Shimobashiric acid C contains two moieties, salvianic acid A and *rel*-(1*R*,2*R*,3*S*,4*S*)-2,4-bis(3,4-dihydroxyphenyl)cyclobutane-1,3-dicarboxylic acid (CBDA-10) (Fig. 1a). However, due to the existence of multiple

^a Department of Physical Sciences, Eastern New Mexico University, Portales, NM 88130, USA. E-mail: zhihan.wang@enmu.edu

^b School of Pharmaceutical Sciences, Jilin University, Changchun, Jilin 130021, China

^c College of Chinese Herbal Medicine, Jilin Agricultural University, Changchun, Jilin 130118, China

† Electronic supplementary information (ESI) available: Statistic data and crystallographic data. CCDC 2021369, 2021371, 2021372 and 2021374. For ESI and crystallographic data in CIF or other electronic format see DOI: 10.1039/d0ce01403f

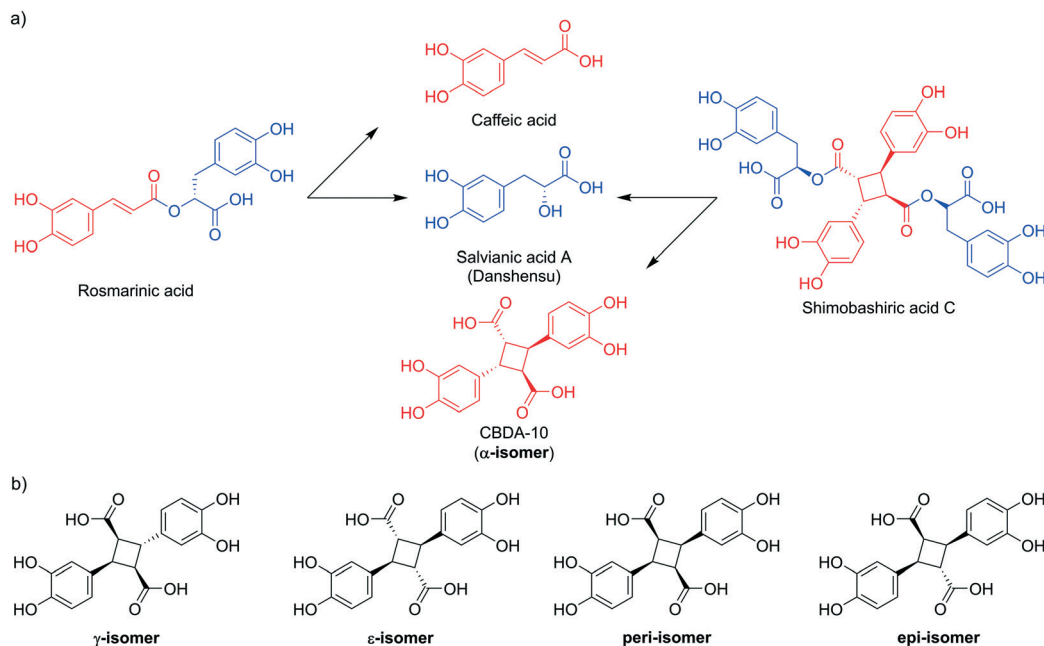


Fig. 1 a) Two caffeic acid derivatives from plant kingdom: rosmarinic acid (caffeic acid + salvianic acid A) and shimobashiric acid C (salvianic acid A + CBDA-10). b) The stereoisomers of CBDA-10.

stereocenters, the synthesis of CBDA-10 is exceptionally arduous using conventional organic synthesis methods.¹¹ Therefore, there are few studies on the biological activities of shimobashiric acid C.^{10b,12}

The challenge in the synthesis of CBDA-10 is to construct the stereospecific cyclobutane, which is the key motif of the CBDA-10. Photon excitation can be used to construct a cyclobutane ring through a $2\pi-2\pi$ cycloaddition reaction, but the excited olefin-containing molecules in the solution may lead to *cis-trans* isomerization and produce a mixture of stereo products.^{11b,c,13} In particular, CBDA-10 has five stereoisomers (Fig. 1b), which brings great obstacles to the preparation of it using the reported methods. This work demonstrates the stereospecific preparation of CBDA-10 using topochemical photocycloaddition reaction. In topochemical reactions, the atoms only proceed with minimal movement, which can avoid side reactions and produce stereospecific products. Topochemical reactions have the advantage of realizing sophisticated structures that are difficult to achieve in conventional organic synthesis. However, the most difficult aspect of topochemical photocycloaddition is to construct the required atomic orientations. The ideal orientation of atoms and the $2\pi-2\pi$ system is that the distance must be in the range of 3.5–4.2 Å, and the reactive double bonds must also be arranged in parallel.¹⁴ Applying crystal engineering strategies to topochemical reactions has the merit of arranging atoms in the desired orientations. Crystal engineering is based on the understanding and use of the weak intermolecular interactions to design and synthesize molecular structures with desired physical and chemical properties.¹⁵ Those weak intermolecular interactions that can be used in crystal

engineering include hydrogen bonds, halogen bonds, van der Waals interactions, dispersion, dipole–dipole interactions, and ion–dipole interactions. Crystal engineering has been widely used in pharmaceutical co-crystals, supramolecular materials, organic polymers, functional materials, *etc.* In this work, we employed Hirshfeld surface analysis and intermolecular interaction 2D fingerprint to guide us in designing proper molecules for topochemical photocycloaddition to construct the desired caffeic acid derivatives.¹⁶

With aid of crystal engineering strategies, especially the intermolecular interaction information provided by Hirshfeld surface analysis and 2D fingerprints, we designed the molecule with ideal atomic orientation for topochemical photocycloaddition and successfully constructed the desired caffeic acid derivatives, dimethyl *rel*-(1*R*,2*R*,3*S*,4*S*)-2,4-bis(3,4-dihydroxyphenyl)cyclobutane-1,3-dicarboxylate (CBDE-10) and CBDA-10. The designed molecule has absorption below 420 nm, while 43% of solar energy is visible light (400 nm to 700 nm). According to the report of the National Renewable Energy Laboratory, the annual average daily solar radiation in the school area is 5.50 to 5.75 kW h m⁻² per day.¹⁷ This free, clean and renewable energy provides a sustainable way to construct our research.¹⁸ Therefore, sunlight was implemented to trigger the topochemical cycloaddition. The sunlight-induced topochemical cycloaddition in this work is solvent-free, metal-free, byproduct-free, high efficiency, and low consumption of external energy. The CBDE-10 demonstrated free radical scavenging and antioxidant activities *in vitro* the biological activity studies. *In silico* study suggested the CBDE-10 is a potential inhibitor of the fatty acid binding proteins. Interestingly, the newly synthesized CBDE-10 exhibited

photodegradable property at 254 nm radiation. The photodegradation properties and thermal stability of CBDE-10 provide possibilities for its application in the field of environmentally friendly degradable polymeric materials.¹⁹ The monomer caffeic acid methyl ester exists in a variety of plants, and existing studies have shown that it can inhibit the growth and development of harmful insects and is an environmentally friendly plant insecticide. In addition, cyclobutane-containing polymers (CBPs) have demonstrated various applications such as UV-shielding materials,^{19c} sustainable materials,²⁰ degradable materials,^{19a,21} self-healing materials,^{19b,22} and photoresponsive materials.²³ The use of CBDE-10 and CBDA-10 as the building blocks of polymeric materials greatly fulfils the call for environmental protection and zero pollution, which is taken from nature and attributed to nature. Moreover, the construction of CBDA-10 paved the way for the total synthesis and further study of the natural product shimobashiric acid C.

Results and discussion

CA is an analogue of cinnamic acid, an example of classical topochemical photocycloaddition.²⁴ We initially tried to perform topochemical photocycloaddition on CA, but even if CA has an absorption of 300 to 385 nm (Fig. S6†), it still showed photostability with ultraviolet radiation (Fig. S5†). When we noticed the photoactivity of CA, we recrystallized CA in a mixed solvent of methanol and water. The single crystal X-ray diffraction structure shows that the double bonds are parallel with each other, and the distance between them is 3.903 Å with 80.16° inner angle (Fig. 2a and b). Despite those conditions falling into the solid-state postulate of photoreaction, the CA single crystal is not photoreactive under 365 nm UV lamp.^{24,25} After further analysis, we noticed that although the double bonds are parallel to each other, there is a 59.32° interfacial angle between the planes α (α') and plane β , which results in 1.991 Å offset between the double bonds on the CA molecules (Fig. 2c and d). This offset causes the p orbitals on the corresponding double bonds to

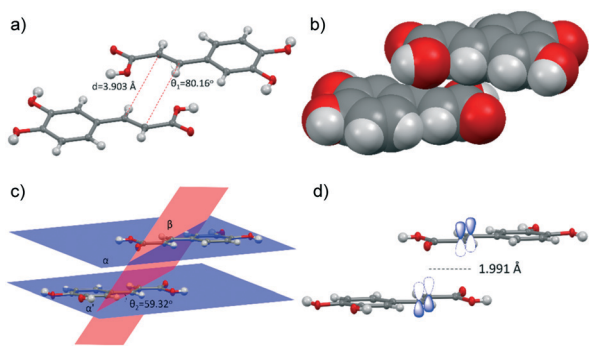


Fig. 2 Single crystal X-ray diffraction of CA. a) & b) The view of closest distance of the two double bonds on CA. c) The interfacial angle between molecular planes α (α') and two double bonds plane β . d) The corresponding p orbitals offset on horizontal line. Oak ridge thermal ellipsoid plot (ORTEP) diagram displayed at 50% probability level.

move away from each other, thereby not forming a new single bond.¹⁴ This offset may be caused by the hydrogen bonds of carboxylic groups, which may weaken the π - π stacking of the double bonds.²⁶ To further understand the interactions between CA molecules, we performed Hirshfeld surface analysis and 2D fingerprint of intermolecular interaction contribution.

Intermolecular interactions are very important in molecular stacking. Hirshfeld surfaces with different properties (for example, d_{norm} , electrostatic potential, shape index, and curvature) are very useful tools for visualizing the interactions between molecules and their contribution to molecular crystal packing behavior.²⁷ On the d_{norm} mapped Hirshfeld surface, the red-blue-white colour scheme is used to distinguish intermolecular interactions in the crystal structure (Fig. 3a). The white surface represents contacts whose distance is equal to the sum of the van der Waals radii. The red region represents shorter distance than sum of van der Waals radii, while blue region represent indicates a

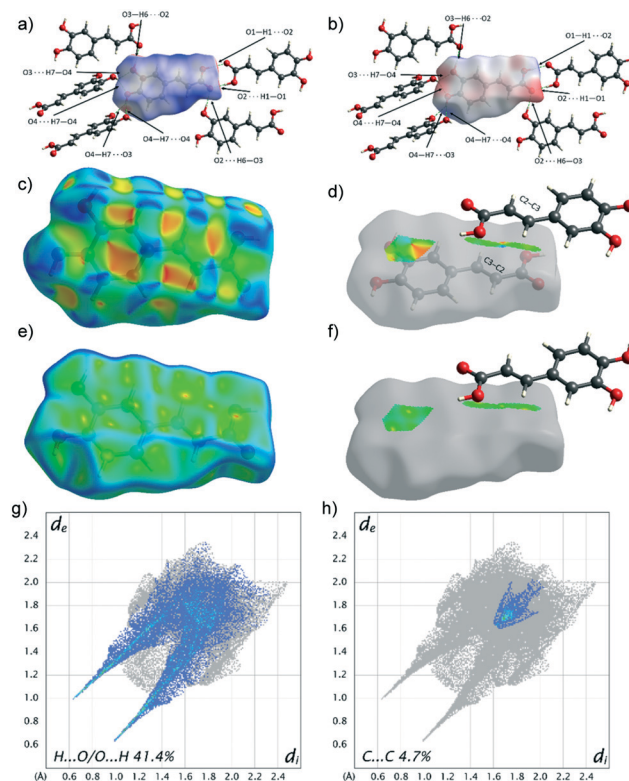


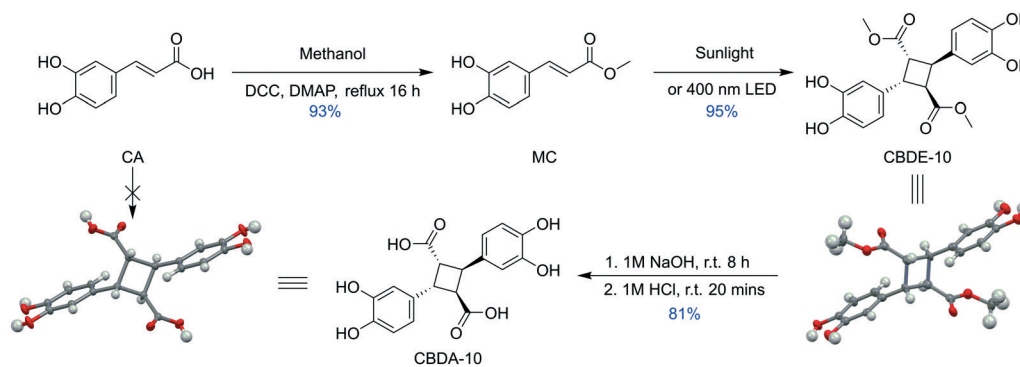
Fig. 3 Hirshfeld surface analysis of CA. a) Hirshfeld surface mapped with d_{norm} visualize the intermolecular interactions. b) Hirshfeld surfaces mapped with electrostatic potential using the 6-311G(d,p) basis set at B3LYP level theory. c) Hirshfeld surfaces mapped over the shape-index of CA. d) Shape-index indicates the π - π interaction between the adjacent CA molecule. e) Hirshfeld surfaces mapped over curvedness of CA. f) Curvedness map indicate the π - π interaction between the adjacent CA molecule. g) $\text{H}\cdots\text{O}/\text{O}\cdots\text{H}$ interaction contribution. h) $\text{C}\cdots\text{C}$ interaction contribution. Note: the green dots lines represent the prominent hydrogen bonds. The pattern of orange and blue triangles in the shape-index represents the π - π interaction. The flat regions on the curvedness indicate the π - π interaction as well.

longer distance than the van der Waals radii. On the electrostatic potential Hirshfeld surface, it is shown as blue and red areas, corresponding to the positive and negative potentials, respectively (Fig. 3b). The blue area (e.g. O1–H1···O2) represents a positive electrostatic potential (hydrogen bond donor), and the red area (e.g. O2···H6–O3) represents a negative electrostatic potential (hydrogen bond acceptor). From Fig. 3a and b, we can clearly see that a CA molecule interacts with five adjacent molecules mainly through hydrogen bonds. The 2D intermolecular interaction fingerprint provides information about intermolecular interactions and their relative contribution to the Hirshfeld surface. The 2D fingerprint obviously shows that the contribution of hydrogen bonds to the interaction between CA molecules is 41.4% (Fig. 3g). The shape index of the Hirshfeld surface is a tool to visualize the π - π interaction through the presence of adjacent orange and blue triangles (Fig. 3c). The blue triangle is the convex region representing the atoms of the molecules inside the surface, while the orange triangle is the concave region associated with the π - π interacting atoms above it. Fig. 3c shows the pattern of alternating orange and blue triangles with appropriate symmetry, indicating an offset π - π interaction with the molecules above it. The π - π interaction can also be observed on the curvedness mapped Hirshfeld surface, which is a flat area on the surface (Fig. 3e). However, the π - π interaction is very weak between C2–C3 and C3–C2 (Fig. 3d and f). This analysis is consistent with the 2D fingerprint which shows the contribution of the C···C interaction is 4.7%. It is shown as an obvious triangle near $d_e = d_i \approx 1.8 \text{ \AA}$, which refers to the characteristic of π - π interaction (Fig. 3h).

According to the intermolecular interaction information provided by Hirshfeld surface and 2D fingerprints of CA, we hypothesize that if an electron-donating group is introduced to the carboxyl group of CA, the hydrogen bond interaction will decrease, and the π - π interaction will be relatively increased, which may result in the ideal atomic orientations for topochemical photocycloaddition. Alkoxy group is a good electron-donating group which have the chance to break the hydrogen bonds. Since the longer the alkoxy chain, the more

flexible the alkoxy chain, the shorter chain is preferred in crystal engineering to maintain the original molecular pattern. Methoxy, ethoxy and propoxy are the idea candidates. To verify our hypothesis, we started from methoxy group. The synthesis was started from Steglich esterification of caffeic acid using *N,N'*-dicyclohexylcarbodiimide (DCC) and 4-dimethylaminopyridine (DMAP) (Scheme 1). The synthesized methyl caffeate (MC) is also a natural product that can be extracted from *Solanum torvum* fruits and is reported to have anticancer activity.²⁸ Additionally, methyl caffeate showed anti-inflammatory activity.²⁹ Once MC was prepared, its single crystal was obtained from ethyl acetate and hexane. The single crystal X-ray diffraction results showed the double bonds are parallel and the distance is 3.654 Å with inner angle 70.39° (Fig. 4a and b). Planes α (α') and plane β have an 86.63° interfacial angle which induced 0.214 Å offset between p orbitals on each double bond (Fig. 4c and d). Now, the orientations of the reactive double bonds fall within the ideal conditions of topochemical photocycloaddition.

In order to elucidate the pattern change along with the influence of methoxy group, a close examination with Hirshfeld surface on MC was performed. Both d_{norm} mapped Hirshfeld surface and electrostatic potential mapped Hirshfeld surface indicate the reduced hydrogens bonds (Fig. 5a and b). One CA molecule has hydrogen bonds with five surrounding CA molecules, while one MC molecule has hydrogen bonds with three surrounding MC molecules (Fig. 5a and b). The 2D fingerprint shows that the contribution of hydrogen bonds to molecular interactions of MC molecules is decreased to 33.1% (Fig. 5g), which is 18.8% lower than that of CA molecules (Fig. 3g). On the other hand, it is easy to observe the π - π interaction related to the adjacent orange and blue triangles in the Hirshfeld surface mapped by the shape index (Fig. 5c). In particular, the π - π interaction between reactive double bonds (C2–C3···C3–C2) is enhanced (Fig. 5d). The curvedness surface shows more flat areas confirming the same observation (Fig. 5e and f). The C···C interaction contribution of MC molecules increased to 7.4%, which also reflects the enhanced π - π interaction (Fig. 5h).



Scheme 1 The designed synthetic route of CBDE-10 and CBDA-10 using crystal engineering guidance. Oak ridge thermal ellipsoid plot (ORTEP) diagram displayed at 50% probability level.

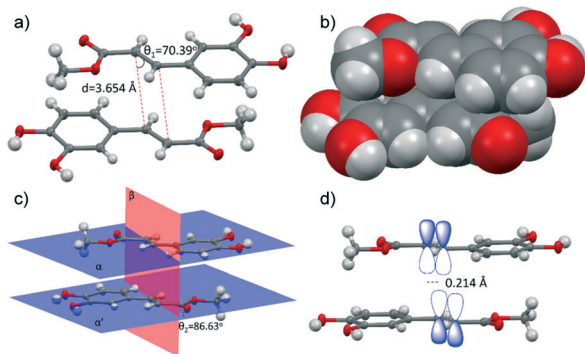


Fig. 4 Single crystal X-ray diffraction of MC. a) & b) The view of closest distance of the two double bonds on MC. c) The interfacial angle between molecular planes α (α') and two double bonds plane β on MC. d) The corresponding p orbitals offset on horizontal line of MC. Oak ridge thermal ellipsoid plot (ORTEP) diagram displayed at 50% probability level.

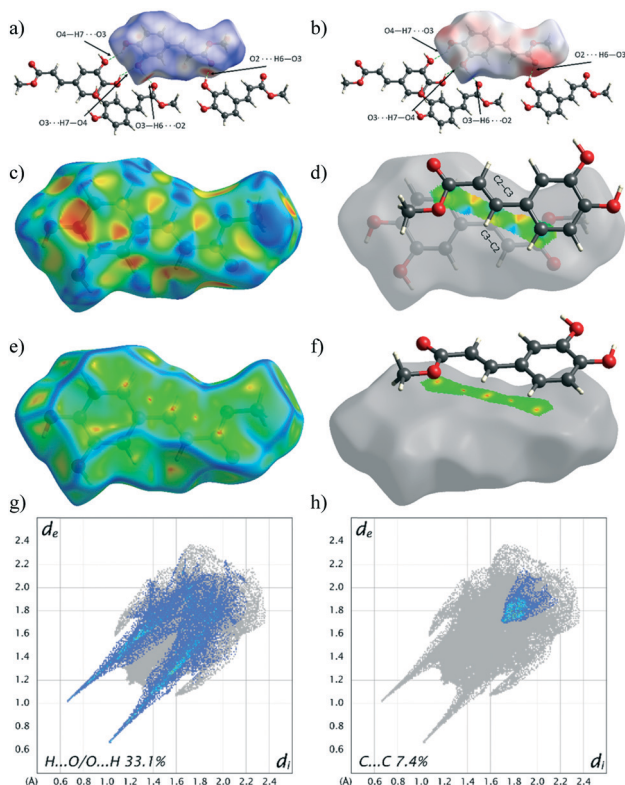


Fig. 5 Hirshfeld surface analysis of MC. a) Hirshfeld surface mapped with d_{norm} visualize the intermolecular interactions. b) Hirshfeld surfaces mapped with electrostatic potential using the 6-311G(d,p) basis set at B3LYP level theory. c) Hirshfeld surfaces mapped over the shape-index of MC. d) Shape-index indicates the π - π interaction between the adjacent MC molecule. e) Hirshfeld surfaces mapped over curviness of MC. f) Curviness map indicate the π - π interaction between the adjacent MC molecule. g) $\text{H}\cdots\text{O}/\text{O}\cdots\text{H}$ interaction contribution. h) $\text{C}\cdots\text{C}$ interaction contribution. Note: the green dots lines represent the prominent hydrogen bonds. The pattern of orange and blue triangles in the shape-index represents the π - π interaction. The flat regions on the curviness indicate the π - π interaction as well.

Once we determined that MC was in the ideal atomic orientation for topochemical photocycloaddition, we started to proceed the photocycloaddition of MC. The electron-donating group not only brings the atoms to ideal orientations, but also makes the bathochromic shift of MC. The solid-state MC has absorption below 420 nm (Fig. S6[†]), which makes it possible to perform topochemical photocycloaddition under visible light. Most of the solar radiation that reaches the earth is visible light that provides clean and renewable free energy for photocycloaddition. Therefore, the solid MC was placed into sunlight (outside the laboratory, 18 h) or underneath a 400 nm light-emitting diode (LED) bulb (in the laboratory, 24 h) for cycloaddition. FT-IR confirmed the completion of the cycloaddition. Infrared spectra showed that the characteristic absorption peak of $\text{C}=\text{O}$ at 1669 cm^{-1} under sunlight shifted to 1705 cm^{-1} due to the deconjugation of the carbonyl group. After the reaction, the stretching of $\text{C}=\text{C}$ (1624 cm^{-1}) disappeared as well as the out-of-plane distortion of the hydrocarbon single bonds in the *trans*- $\text{CH}=\text{CH}$ (970 cm^{-1}). The solvent-free photocycloaddition showed high efficiency with a yield of 95%. The remaining 5% may be attributable to the sublimation of MC, because when molecules absorb photons, they may generate heat. The structure of CBDE-10 was confirmed by ^1H -, COSY-, ^{13}C -, and DEPT90-NMR. ^1H -NMR spectra showed that the double bond peaks at 7.49 (d) and 6.27 (d) ppm faded in the sunlight. The peaks at 3.70 (dd) and 4.07 (dd) ppm corresponding to the sp^3 -hybridized carbons in the newly formed cyclobutane ring indicate that CBDE-10 possesses an α -stereoisomer structure.³⁰ The 46.83 and 40.89 ppm peaks in DEPT90-NMR also provide evidence of newly formed cyclobutane rings. The stereocenters were further confirmed by the single crystal analysis which was obtained from methanol and dimethylformamide (Scheme 1). The results proved the stereospecific preparation of the α -isomer. Besides, no side reactions and by-products were observed which also proved the efficiency of the topochemical photocycloaddition. The cyclobutane moiety possesses a coplanar conformation with 88.68° inner angle and 0.00° torsion. The precursor of shimobashiric acid C was successfully prepared by the hydrolysis of CBDE-10 and the single crystal analysis of CBDA-10 showed the same cyclobutane moiety as CBDE-10 (Scheme 1). Both results suggested that the stereocenters on the CBDE-10 and CBDA-10 are *rel*-($1\alpha, 2\alpha, 3\beta, 4\beta$) proving the stereospecific synthesis strategy in topochemical photocycloaddition. After refining the method of synthesis, we studied bioactivities including radical scavenging, antioxidant and *in silico* protein binding.

Free radicals are atoms or molecules with highly reactive unpaired electrons. They can be produced naturally in the body during normal cellular metabolism, or they can be introduced from the environment.³¹ However, the uncontrolled generation of free radicals can damage the main components of cells, such as DNA, proteins, lipid membranes, and carbohydrates.³¹ Those damages may cause various adverse reactions such as cancer, atherosclerosis,

central nervous system diseases, autoimmune diseases, heart diseases, diabetes, and cardiovascular disease.³¹ Studies have shown that the anticancer activities of CA and its derivatives are linked to their antioxidant properties. This can be attributed to the prevention of cellular damage induced by free radicals.^{28b,32} Herein, we investigated the *in vitro* radical scavenging and antioxidative activities of compounds CA, MC, and CBDE-10. Their free-radical-scavenging activities were assessed by their activity against a stable free radical 2,2-diphenyl-1-picrylhydrazyl (DPPH).³³ DPPH is a stable organic radical with a purple colour and a strong absorption at 517 nm. Their antioxidant activities were investigated using lipid peroxidation of linoleic acid emulsion system and ferric thiocyanate assay.^{32a,33} The free radical scavenging activities of compound CA, MC, and CBDE-10 were studied by measuring the absorbance decrease at 517 nm within 30 min. The results showed that the scavenging rate of free radicals for CA, MC, and CBDE-10 is about 90% at 50 $\mu\text{g mL}^{-1}$ (Fig. 6a). As the concentration increased, the efficiency of free radicals scavenging increased. The inset of Fig. 6a shows the colour change of the inhibitions in different concentrations of CBDE-10. Meanwhile, we studied the kinetics of the free radical scavenging, and the results showed the radical scavenging reached the highest rate in 5 min (Fig. S8†). Fig. 6b showed the results of antioxidative activity. In the process of linoleic acid peroxidation, the produced peroxide can oxidize Fe^{2+} to Fe^{3+} , and then Fe^{3+} ion forms a red complex $[\text{Fe}(\text{SCN})]^{2+}$, which has a maximum absorption at 500 nm. Therefore, high absorbance indicates high oxidation. The results showed that all samples had a decent inhibitory effect on the oxidation of the lipid, especially MC, which was better than CA and CBDE-10 in antioxidant study. The above studies indicated that the caffeic acid derivatives are promising radical scavenging agents and antioxidants.

Fatty acid-binding protein (FABP) is composed of a group of proteins that coordinate lipid transport and responses, which can be found in the brain, liver, heart, intestine, testis, adipocyte, epidermis, and myelin. FABPs play an important role in metabolic pathways, regulating gene expression and cell growth.³⁴ It is believed that FABPs are related to the proliferation and apoptosis of cancer cells.³⁵ For example,

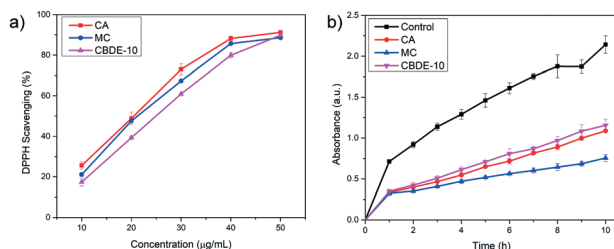


Fig. 6 a) Scavenging effect of CA, MC, and CBDE-10 on the stable DPPH at different concentrations (10–50 $\mu\text{g mL}^{-1}$). Inset: The radical scavenging results of 3 after 30 min. b) Antioxidant study of CA, MC, and CBDE-10 (20 $\mu\text{g mL}^{-1}$) in 10 h using lipid peroxidation assay.

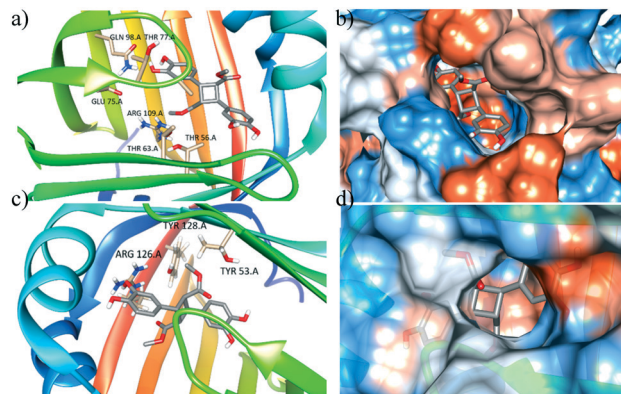


Fig. 7 The *in silico* study of CBDE-10 binding with FABP5 and FABP7. a) & c) The interactions between CBDE-10 and FABP5/FABP7. b) & d) The surface model of the docking site which shows the CBDE-10 fit the pockets of FABP5 and FABP7.

FABP5-related-signalling transduction pathway involves in the prostate tumour promotion.³⁶ FABP7, also known as brain FABP, plays a pivotal role in HER2+ breast cancer brain metastasis.³⁷ Hence, we studied the binding affinity of CBDE-10 and FABP5(PDB: 4LKT)/FABP7(PDB: 1FE3). The *in silico* study was carried out using Autodock Vina program using the crystalline data of CBDE-10 as the docking ligand (Fig. 7).³⁸ The results showed that the maximum docking score of CBDE-10 in FABP5 was $-8.1 \text{ kcal mol}^{-1}$ and the maximum docking score of CBDE-10 in FABP7 was $-7.6 \text{ kcal mol}^{-1}$. Fig. 7 visualized the docking results which showed the interactions between CBDE-10 and the amino acids on FABP5 and FABP7.³⁹ CBDE-10 has the potential to be a lead compound or an inhibitor of FABP5 and FABP7.

An additional finding, compound CBDE-10 can be steadily degraded under 254 nm radiation. In 30 min of radiation, 96% of compound CBDE-10 was degraded (Fig. 8a). This special property makes CBDE-10 a degradable building block for polymeric materials. Polymeric plastics not only bring great benefits to society, but also threaten the environment due to the plastic pollutions. Compound CBDE-10 has the potential to build photodegradable plastics. In addition, thermogravimetric analysis demonstrated the thermostability of CBDE-10, which showed the maximum decomposition occurred at 328 $^{\circ}\text{C}$ (Fig. 8b). The $T_{5\%}$ and $T_{10\%}$ occurred at

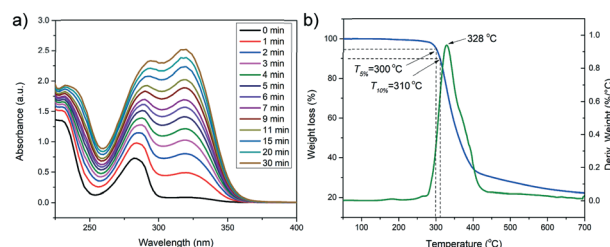


Fig. 8 a) The degradation of CBDE-10 at 254 nm in 30 min. b) Thermogravimetric analysis of CBDE-10 from 50 $^{\circ}\text{C}$ to 700 $^{\circ}\text{C}$ at 20 $^{\circ}\text{C min}^{-1}$ heating rate under N_2 atmosphere.

300 °C and 310 °C, respectively, which also indicated CBDE-10 is suitable to be a backbone in thermoplastics.

Conclusion

In conclusion, we demonstrated how to apply crystal engineering strategies into molecular stacking as well as how to use free, clean, and renewable solar energy into solvent-free cycloaddition to construct caffeic acid derivatives. Based on the intermolecular interaction information provided by Hirshfeld surface and 2D fingerprints, we designed the photoreactive monomer. In the synthesis process, sunlight or 400 nm LED was employed as the light source, which indicates the application of clean renewable energy to drug discovery and polymeric materials. One of the five stereoisomers of CBDA-10 was successfully prepared. No by-products or other stereoisomers were observed, proving the high efficiency of topochemical cycloaddition reaction. Meanwhile, solar energy was harvested and stored into chemical bonds. The synthesized caffeic acid derivatives possess biological activities of scavenging free radicals and antioxidants. In particular, CBDE-10 showed the potential inhibitory activity of fatty acid binding proteins in molecular simulations, which offered a new lead compound for the development of FABPs inhibitors. The photodegradable properties CBDE-10 may provide a new way for the degradable polymeric materials. On the other hand, the CBDA-10 affords the core scaffold of the natural product shimobashiric acid C, paving the way of the total synthesis. Using CBDA-10 or CBDE-10 as the lead compound or building block achieves the goal of “nature-to-nature” in green chemistry.

Experimental section

Materials

All chemicals and solvents were purchased from Alfa-Aesar (caffeic acid 98+%, *N,N'*-dicyclohexylcarbodiimide 99%, ethyl acetate environmental grade 99.5+%), TCI Chemicals (4-dimethylaminopyridine >99%, 1,1-diphenyl-2-picrylhydrazyl radical 97+%, 2,2'-azobis(2-methylpropionamide) dihydrochloride 98%, linoleic acid 99%), MilliporeSigma (acetonitrile HPLC grade, methanol HPLC grade), VWR Chemicals BDH (sodium hydroxide ACS grade), VWR (Tween 20 polysorbate proteomics grade), Acros Organics (ammonium thiocyanate 99+% extra pure, iron(II) chloride tetrahydrate 99+%), Innovating Science (sodium chloride reagent grade, sodium sulfate anhydrous lab grade, phosphate buffered saline lab grade, PBS buffer pH 7.0 lab grade, 1.0 M hydrochloric acid solution lab grade), Beantown Chemical Corporation (ethyl acetate ACS 99.5% min), Thermo Fisher Scientific (hexanes ACS grade), Best Value Vacs (hexanes high purity lab grade), Decon Labs, Inc. (ethanol 190 proof), or Cambridge Isotope Laboratories, Inc. (deuterium solvents) and used without further purification. Borosilicate glass vial used in the photoreaction were purchased from VWR (66022-106). The light source used

for the topochemical photocycloaddition and degradation were sunlight, an 11 W hocinderal LED bulb (wavelength: 400 nm) and a Philips G15T8 Germicidal lamp (wavelength: 254 nm). Sonication was carried out in a BRANSON 2800 digitally heated timer-adjustable ultrasonic cleaner or Fisher Scientific FS-14 Solid State/Ultrasonic Cleaner. Centrifuge used in this study was Fisher Scientific Centrifric Model 228.

Synthesis of MC

Caffeic acid (2.0 g, 11 mmol), *N,N'*-dicyclohexylcarbodiimide (DCC, 2.7 g, 13 mmol), and 4-dimethylaminopyridine (DMAP, 0.1 g, 1 mmol) were added to 15 mL of methanol in a 50 mL round bottom flask. The mixture was kept stirring and refluxed for 16 h. After reaction, the mixture was cooled down to room temperature. The side product dicyclohexylurea (DCU) was filtered through filter paper and the solid was washed with ethyl acetate 50 mL for twice. Then the filtrate was washed with 1 M HCl 50 mL and then with brine 50 mL in a 125 mL separatory funnel. The organic layer was concentrated to give a yellow crude product. The crude product was dissolved into 30 mL ethyl acetate and charged with 90 mL of hexane. The suspension was filtered through a 10 cm silica gel column. The column was eluted twice using mixed 30 mL ethyl acetate and 60 mL hexane. TLC showed all samples were collected. The combined collections were concentrated by roller evaporator to give a white product 2 (2.0 g, 93%). ¹H NMR (400 MHz, DMSO-*d*₆) δ 9.36 (s, 2H), 7.49 (d, *J* = 15.9 Hz, 1H), 7.06 (s, 1H), 7.00 (d, *J* = 8.0 Hz, 1H), 6.77 (d, *J* = 7.9 Hz, 1H), 6.27 (d, *J* = 15.9 Hz, 1H), 3.69 (s, 3H) ppm. ¹³C NMR (126 MHz, DMSO-*d*₆) δ 167.47, 148.87, 146.02, 145.63, 125.93, 121.88, 116.17, 115.23, 114.12, 51.67 ppm. MS (*m/z*): [M + Na]⁺ calcd. for C₁₀H₁₀O₄Na⁺, 217.047; found 217.046. IR: ν = 3473, 3086, 3033, 2953, 2918, 1669, 1624, 1604, 1535, 1435, 1305, 1293, 1240, 1179, 1159, 1111 cm⁻¹.

Visible light topochemical cycloaddition of CBDE-10

500 mg powder of MC was scattered on a 5" × 5" glass slide and placed in sunlight or underneath 400 nm LED with 1 cm distance for radiation (18–24 h). The powder was flipped over every 3 h until FT-IR showed the completion of the reaction. Another alternative method can be used as well. 1.0 g of MC was suspended into 15 mL deionized water in a 20 mL vial. The suspension was put in front a LED with 1 cm distance. The mixture was stirred and irradiated at room temperature for 18 h. FT-IR was used to monitor the photoreaction. Once FT-IR showed the completion of the photoreaction, the mixture was filtered through a filter paper to give CBDE (0.95 g, 95%) as a white powder. ¹H NMR (500 MHz, DMSO-*d*₆) δ 8.81 (d, *J* = 23.8 Hz, 4H), 6.65 (d, *J* = 8.3 Hz, 4H), 6.52 (dd, *J* = 8.2, 2.2 Hz, 2H), 4.07 (dd, *J* = 10.4, 7.2 Hz, 2H), 3.70 (dd, *J* = 10.4, 7.2 Hz, 2H), 3.29 (s, 6H) ppm. ¹³C NMR (126 MHz, DMSO-*d*₆) δ 172.42, 145.37, 144.56, 130.00, 118.58, 115.77, 115.27, 51.63, 46.83, 40.89 ppm. MS (*m/z*): [M + Na]⁺ calcd. for C₂₀H₂₀O₈Na⁺, 411.105; found 411.105. IR: ν = 3384, 3320, 1705, 1616, 1537, 1446, 1359, 1258, 1237, 1196, 1178 cm⁻¹.

Synthesis of CBDA-10

The 0.2 g of CBDE-10 was added to 5 mL of water. A 1 M solution of NaOH 0.2 g in 5 mL water was added dropwise to the sample mixture. The mixture was stirred at room temperature for 8 h. Then the mixture was poured into 10 mL 1 M HCl. The precipitate was filtered. The filtrate was extracted with 20 mL ethyl acetate for twice. The combined organic layers were dried over sodium sulfate and filtered through a 10 cm silica gel column. The collections were concentrated to give CBDA-10 (0.15 g, 81%) as a white solid. ^1H NMR (500 MHz, $\text{DMSO-}d_6$) δ 11.98 (s, 2H), 8.77 (d, $J = 37.6$ Hz, 4H), 6.67 (d, $J = 2.1$ Hz, 2H), 6.64 (d, $J = 8.1$ Hz, 2H), 6.54 (dd, $J = 8.2, 2.1$ Hz, 2H), 4.00 (dd, $J = 10.4, 7.2$ Hz, 2H), 3.58–3.51 (dd, $J = 10.4, 7.2$ Hz, 2H). ^{13}C NMR (126 MHz, $\text{DMSO-}d_6$) δ 173.54, 145.28, 144.48, 130.78, 118.83, 115.70, 115.46, 47.19, 40.95. MS (m/z): $[\text{M} + \text{Na}]^+$ calcd. for $\text{C}_{18}\text{H}_{16}\text{O}_8\text{Na}^+$, 383.073, found 383.073. IR: $\nu = 3253, 1689, 1608, 1513, 1440, 1349, 1283, 1203, 1112$ cm^{-1} .

Crystallization of CA, MC, CBDE-10, and CBDA-10

CA (200 mg) was dissolved in 5 mL of methanol and 1 mL of water. The mixture was sonicated for 30 min and filtered into a 20 mL glass vial. The vial was placed uncovered into a fume hood. High-quality single crystals were obtained in about three days.

MC (100 mg) was mixed with 15 mL of hexane and 5 mL of ethyl acetate, sonicated for 30 minutes, and then filtered into a 20 mL glass vial. The vial was exposed in a fume hood without cover. Cubic shape crystals were obtained in about two days.

CBDE-10 (35 mg) was mixed with 10 mL of methanol and 1 mL of dimethylformamide, sonicated for 30 minutes, and then filtered into a 20 mL glass vial. The vial was exposed in a fume hood without cover. High-quality single crystals were obtained in about seven days.

CBDA-10 (20 mg) was mixed with 10 mL of ethyl acetate and filtered into a 20 mL glass vial. The vial was exposed in a fume hood without cover. Cubic shape crystals were obtained in about two days. CBDA10-co-EA ^1H NMR (500 MHz, $\text{DMSO-}d_6$) δ 11.98 (s, 2H), 8.77 (d, $J = 37.7$ Hz, 4H), 6.67 (d, $J = 2.1$ Hz, 2H), 6.64 (d, $J = 8.1$ Hz, 2H), 6.54 (dd, $J = 8.2, 2.1$ Hz, 2H), 4.05–3.96 (m, 5H), 3.55 (dd, $J = 10.4, 7.2$ Hz, 2H), 1.98 (s, 4H), 1.16 (t, $J = 7.1$ Hz, 4H) ppm. ^{13}C NMR (126 MHz, $\text{DMSO-}d_6$) δ 173.54, 170.82, 145.28, 144.48, 130.78, 118.82, 115.70, 115.45, 60.23, 47.18, 40.95, 21.52, 21.23, 14.54.

Characterization

Ultraviolet-visible (UV-vis) spectra were recorded on a Thermo Scientific™ GENESYS™ 50 UV-visible spectrophotometer with a 3.5 mL quartz cuvette. Melting points were measured on a Stanford Research Systems (SRS) melting point apparatus MPA100 automated melting point system without correction. Nuclear magnetic resonance (NMR) spectra were recorded on a JEOL ECS 400 MHz NMR spectrometer at 400 MHz (^1H) or Varian Unity Inova 500 spectrometer operating

at 500 MHz (^1H) and 126 MHz (^{13}C). ^1H NMR data were reported as follows: chemical shift (ppm), s = singlet, d = doublet, t = triplet, q = quartet, dd = doublet of doublets, m = multiplet, coupling constant (Hz), and integration. Deuterated solvents were used: dimethyl sulfoxide ($\text{DMSO-}d_6$). Fourier transform infrared (FT-IR) spectra were acquired with a wavenumber range of 400–4000 cm^{-1} on a Thermo Scientific Nicolet iS10 FT-IR spectrometer. High-resolution mass spectrometry (HRMS) was performed on a Waters SYNAPT G2Si with electrospray ionization (ESI) source. Thermogravimetric analysis (TGA) was performed on a TA Instruments SDT Q5000 at a ramp rate of 20 $^\circ\text{C min}^{-1}$ from 50 $^\circ\text{C}$ to 700 $^\circ\text{C}$ in nitrogen constant flow of 100 mL min^{-1} . Single-crystal X-ray data were collected on a Rigaku XtaLAB Synergy-i Kappa diffractometer equipped with a PhotonJet-i X-ray source operated at 50 W (50 kV, 1 mA) to generate Cu $\text{K}\alpha$ radiation ($\lambda = 1.54178$ Å) and a HyPix-6000HE HPC detector or a Bruker Apex or Bruker Kappa Apex II Duo X-ray diffractometer with Mo $\text{K}\alpha$ ($\lambda = 0.71073$ Å) or Cu $\text{K}\alpha$ ($\lambda = 1.54178$ Å). The structures were solved by direct methods and refined by the full-matrix least-squares technique using the SHELXL-2014 package.

1,1-Diphenyl-2-picrylhydrazyl (DPPH) scavenging assay

A 0.2 mg mL^{-1} DPPH' ethanol solution was prepared, and 1 mL of this solution was added to 1 mL of sample solutions with different ethanol concentrations (10–50 $\mu\text{g mL}^{-1}$). After 30 minutes, the absorbance was measured at 517 nm. The scavenge efficiency of the DPPH' radical was calculated using the following equation: DPPH' scavenging effect (%) = $(A_{\text{Control}} - A_{\text{Sample}})/A_{\text{Control}} \times 100$. A_{Control} is the absorbance of the control reaction and A_{Sample} is the absorbance in the presence of samples. All tests were repeated three times.

Determination of antioxidant activity in a linoleic acid system

A linoleic acid emulsion was prepared by mixing 0.28 g of linoleic acid, 0.28 g of Tween 20 as an emulsifier, and 50 mL of phosphate buffer (0.2 M, pH 7.0). A 0.5 mL ethanol solution of different samples (20 $\mu\text{g mL}^{-1}$) was mixed with linoleic acid emulsion (1 mL, 0.2 M, pH 7.0) and phosphate buffer (0.5 mL, 0.2 M, pH 7.0). The samples were placed into 15 mL centrifuge tubes separately. The control sample contained 1 mL of emulsion, 0.5 mL of PBS buffer, and 0.5 mL of ethanol. The peroxidation was initiated by adding AAPH solution (0.1 M, 50 μL). All samples were vortexed for 1 min. The reaction mixture was incubated in the dark at 37 $^\circ\text{C}$ to accelerate peroxidation. The absorbance at 500 nm was measured every hour. According to the thiocyanate method, the levels of peroxidation were determined by sequentially adding ethanol (2 mL, 75%), ammonium thiocyanate (0.1 mL, 30%), sample solution (0.1 mL, 20 $\mu\text{g mL}^{-1}$), and ferrous chloride (0.1 mL, 20 mM in 3.5% HCl). After 3 min, the peroxide value was determined by reading the absorbance at

500 nm on a UV-vis spectrometer. All tests were repeated three times.

Statistical analysis

All experiments were performed in triplicate. The data were recorded as expressed as the mean of three replicate determinations and standard deviation. Multiple comparisons were performed by one-way analysis of variance (ANOVA), followed by least significant difference procedure. *p*-Values < 0.05 were considered as significant and *p*-values < 0.01 were regarded as very significant.

Photodegradation of CBDE-10

3 mL of CBDE-10 (40 $\mu\text{g mL}^{-1}$ in acetonitrile) was transferred into a quartz cuvette. The cuvette was placed 10 cm away from the UV lamp (254 nm). The absorbance was measured by UV-vis spectrometer in 30 min. The degradation level was calculated *via* the calibration curve determined by linear regression ($R^2 = 0.997$).

Molecular docking

Macromolecule target structures, FABP-5 (4LKT, 2.57 Å Res. crystal structure of human epidermal fatty acid binding protein) and FABP-7 (1FE3, 2.80 Å Res. crystal structure of human brain fatty acid binding protein oleic acid), were obtained using the RCSB Protein Data Banks and the ligand PDB structure of interest was obtained from XRD characterization. After restricting the proteins of interest to strictly A chains, standard processing was then used to obtain the respective PDBQT files for analysis *via* Autodock Vina. Parameters used moderate exhaustiveness (>8), keeping all others in default states. Each was only found to contain the binding site of the previously bound active site for each respective protein; thus, the grid coordinates were centered around these active sites while encompassing the entire protein section due to its relatively small size. Validation of poses was achieved by ensuring the database ligands could be redocked to their corresponding protein under the established parameters.

Hirshfeld surface computational method

Hirshfeld surface along with the 2D fingerprint plots for compounds were generated with the aid of the CRYSTALEXPLORER 17.5 software.⁴⁰ Hirshfeld surface and 2D fingerprints can be used to quantify the properties of molecular interactions in lattices. The d_{norm} is a function of the distance between the internal (d_i) and external (d_e) nuclei (atoms) of the Hirshfeld surface with respect to the corresponding van der Waals radius. The intermolecular distance information on the surface can be displayed in the 2D histogram of d_e and d_i . This is the unique identifier of the molecules in the crystal structure and is called a fingerprint. The three-dimensional d_{norm} surfaces of CA were plotted over a fixed colour scale of -0.7242 au (red)-1.2806 au (blue). Electrostatic potential was plotted in

scale of -0.0910 au (red)-0.2539 au (blue). Shape index plots were mapped in the colour range -1.000 au (concave) to 1.000 au (convex), and the curvedness in the range of -4.0000 au (flat)-4.000 au (singular). The three-dimensional d_{norm} surfaces of MC were plotted over a fixed colour scale of -0.7436 au (red)-1.2760 au (blue). Electrostatic potential was plotted in scale of -0.0843 au (red)-0.2618 au (blue). Shape index plots were mapped in the colour range -1.000 au (concave) to 1.000 au (convex), and the curvedness in the range of -4.0000 au (flat)-0.4000 au (singular).

Conflicts of interest

There are no conflicts to declare.

Acknowledgements

This work was supported by an Institutional Development Award from the National Institute of General Medical Sciences of the National Institutes of Health (P20GM103451) and Faculty Research and Instructional Development (FRID) grant from the Eastern New Mexico University. The authors acknowledge Dr. Angel Ugrinov at North Dakota State University and Dr. Daniel Unruh at Texas Tech University for the single crystal X-ray diffraction assistance, and Dr. Piotr Dobrowolski at Texas Tech University for the NMR assistance.

References

- (a) A. L. Harvey, *Drug Discovery Today*, 2008, **13**, 894-901; (b) J. A. Beutler, *Curr. Protoc. Pharmacol.*, 2009, **46**, 9.11.11-19.11.21; (c) Y. Xu, F. Wang, H. Guo, S. Wang, S. Ni, Y. Zhou, Z. Wang, H. Bao and Y. Wang, *Molecules*, 2019, **24**, 2355; (d) Y. Wang, L. Wang, Y. Hu, L. Zhang and Z. Wang, *Nat. Prod. Res.*, 2010, **24**, 1518-1522; (e) Z. Wang, B. Kastern, K. Randazzo, A. Ugrinov, J. Butz, D. W. Seals, M. P. Sibi and Q. R. Chu, *Green Chem.*, 2015, **17**, 4720-4724.
- W. Boerjan, J. Ralph and M. Baucher, *Annu. Rev. Plant Biol.*, 2003, **54**, 519-546.
- (a) M. Touaibia, J. Jean-Francois and J. Doiron, *Mini-Rev. Med. Chem.*, 2011, **11**, 695; (b) K. Sidoryk, A. Jaromin, N. Filipczak, P. Cmoch and M. Cybulski, *Molecules*, 2018, **23**, 2199; (c) H. Tang, X. Yao, C. Yao, X. Zhao, H. Zuo and Z. Li, *Sci. Rep.*, 2017, **7**, 7599; (d) K. M. M. Espindola, R. G. Ferreira, L. E. M. Narvaez, A. C. R. Silva Rosario, A. H. M. da Silva, A. G. B. Silva, A. P. O. Vieira and M. C. Monteiro, *Front. Oncol.*, 2019, **9**, 541; (e) J.-W. Yuan, H.-Y. Qiu, P.-F. Wang, J. Makawana, Y.-A. Yang, F. Zhang, Y. Yin, J. Lin, Z.-C. Wang and H.-L. Zhu, *Molecules*, 2014, **19**, 7269.
- Z. Zhang, D. Wang, S. Qiao, X. Wu, S. Cao, L. Wang, X. Su and L. Li, *Sci. Rep.*, 2017, **7**, 4508.
- J. Wu, C. Omene, J. Karkoszka, M. Bosland, J. Eckard, C. B. Klein and K. Frenkel, *Cancer Lett.*, 2011, **308**, 43-53.
- Z. G. G. Ozturk, S. Akyol, G. Erden, A. Gurel and O. Akyol, *Riv. Eur. Sci. Med. Farmacol.*, 2012, **16**, 2064-2068.
- (a) D. C. Hao, X.-J. Gu and P. G. Xiao, in *Medicinal Plants*, ed. D. C. Hao, X.-J. Gu and P. G. Xiao, Woodhead Publishing,

- 2015, pp. 531–585; (b) J. Ren-Wang, L. Kit-Man, H. Po-Ming, C. W. M. Thomas, W. Kam-Sang and F. Kwok-Pui, *Curr. Med. Chem.*, 2005, **12**, 237–246.
- 8 (a) M. Nadeem, M. Imran, T. Aslam Gondal, A. Imran, M. Shahbaz, R. Muhammad Amir, M. Wasim Sajid, T. Batool Qaisrani, M. Atif, G. Hussain, B. Salehi, E. Adrian Ostrander, M. Martorell, J. Sharifi-Rad, W. C. Cho and N. Martins, *Appl. Sci.*, 2019, **9**, 3139; (b) M. L. Scarpatti, *Rice Sci.*, 1958, **28**, 2329–2333.
- 9 (a) J. Stansbury, *J. Restor. Med.*, 2014, **3**, 121–126; (b) C. Luo, L. Zou, H. Sun, J. Peng, C. Gao, L. Bao, R. Ji, Y. Jin and S. Sun, *Front. Pharmacol.*, 2020, **11**, 153; (c) T. Hase, S. Shishido, S. Yamamoto, R. Yamashita, H. Nukima, S. Taira, T. Toyoda, K. Abe, T. Hamaguchi, K. Ono, M. Noguchi-Shinohara, M. Yamada and S. Kobayashi, *Sci. Rep.*, 2019, **9**, 8711.
- 10 (a) T. Murata, T. Miyase and F. Yoshizaki, *Chem. Pharm. Bull.*, 2012, **60**, 121–128; (b) Y.-S. Chen, H.-M. Yu, J.-J. Shie, T.-J. R. Cheng, C.-Y. Wu, J.-M. Fang and C.-H. Wong, *Bioorg. Med. Chem.*, 2014, **22**, 1766–1772; (c) J. Krzyżanowska-Kowalczyk, Ł. Pecio, J. Mołdoch, A. Ludwiczuk and M. Kowalczyk, *Molecules*, 2018, **23**, 2277.
- 11 (a) M. Wang and P. Lu, *Org. Chem. Front.*, 2018, **5**, 254–259; (b) S. K. Pagire, A. Hossain, L. Traub, S. Kerres and O. Reiser, *Chem. Commun.*, 2017, **53**, 12072–12075; (c) T. Lei, C. Zhou, M. Y. Huang, L. M. Zhao, B. Yang, C. Ye, H. Xiao, Q. Y. Meng, V. Ramamurthy, C. H. Tung and L. Z. Wu, *Angew. Chem., Int. Ed.*, 2017, **56**, 15407–15410.
- 12 A. Fujiwara, M. Nishi, S. Yoshida, M. Hasegawa, C. Yasuma, A. Ryo and Y. Suzuki, *Phytochemistry*, 2016, **122**, 139–145.
- 13 T. B. Nguyen and A. Al-Mourabit, *Photochem. Photobiol. Sci.*, 2016, **15**, 1115–1119.
- 14 V. Ramamurthy and K. Venkatesan, *Chem. Rev.*, 1987, **87**, 433–481.
- 15 (a) G. R. Desiraju, *J. Am. Chem. Soc.*, 2013, **135**, 9952–9967; (b) K. Biradha and R. Santra, *Chem. Soc. Rev.*, 2013, **42**, 950–967.
- 16 (a) M. A. Spackman and D. Jayatilaka, *CrystEngComm*, 2009, **11**, 19–32; (b) M. A. Spackman and J. J. McKinnon, *CrystEngComm*, 2002, **4**, 378–392.
- 17 M. Sengupta, Y. Xie, A. Lopez, A. Habte, G. Maclaurin and J. Shelby, *Renewable Sustainable Energy Rev.*, 2018, **89**, 51–60.
- 18 A. Albini and M. Fagnoni, *ChemSusChem*, 2008, **1**, 63–66.
- 19 (a) H. Amjaour, Z. Wang, M. Mabin, J. Puttkammer, S. Busch and Q. R. Chu, *Chem. Commun.*, 2019, **55**, 214–217; (b) M. Abdallah, C. Yoshikawa, M. T. W. Hearn, G. P. Simon and K. Saito, *Macromolecules*, 2019, **52**, 2446–2455; (c) L. Ding, L. Liu, Y. Chen, Y. Du, S. Guan, Y. Bai and Y. Huang, *Chem. Eng. J.*, 2019, **374**, 1317–1325.
- 20 (a) Z. Wang, M. Scheuring, M. Mabin, R. Shahni, Z. D. Wang, A. Ugrinov, J. Butz and Q. R. Chu, *ACS Sustainable Chem. Eng.*, 2020, **8**, 8909–8917; (b) R. K. Shahni, M. Mabin, Z. Wang, M. Shaik, A. Ugrinov and Q. R. Chu, *Polym. Chem.*, 2020, **11**, 6081–6090; (c) Z. D. Wang, Q. Elliott, Z. Wang, R. A. Setien, J. Puttkammer, A. Ugrinov, J. Lee, D. C. Webster and Q. R. Chu, *ACS Sustainable Chem. Eng.*, 2018, **6**, 8136–8141; (d) Z. Wang, K. Randazzo, X. Hou, J. Simpson, J. Struppe, A. Ugrinov, B. Kastern, E. Wysocki and Q. R. Chu, *Macromolecules*, 2015, **48**, 2894–2900; (e) Y. Lie, A. Pellis, I. Funes-Ardoiz, D. Sampedro, D. J. Macquarrie and T. J. Farmer, *ChemSusChem*, 2020, **13**, 4140–4150.
- 21 H. Zhang, X. Li, Y. Lin, F. Gao, Z. Tang, P. Su, W. Zhang, Y. Xu, W. Weng and R. Boulatov, *Nat. Commun.*, 2017, **8**, 1147.
- 22 J. Stouten, D. E. P. Vanpoucke, G. Van Assche and K. V. Bernaerts, *Macromolecules*, 2020, **53**, 1388–1404.
- 23 (a) H. Wang, W. Miao, F. Wang and Y. Cheng, *Biomacromolecules*, 2018, **19**, 2194–2201; (b) M. A. Azagarsamy, D. D. McKinnon, D. L. Alge and K. S. Anseth, *ACS Macro Lett.*, 2014, **3**, 515–519.
- 24 M. D. Cohen, G. M. J. Schmidt and F. I. Sonntag, *J. Chem. Soc.*, 1964, 2000–2013.
- 25 (a) G. M. J. Schmidt, *Pure Appl. Chem.*, 1971, **27**, 647–678; (b) Z. Wang, B. Miller, J. Butz, K. Randazzo, Z. D. Wang and Q. R. Chu, *Angew. Chem., Int. Ed.*, 2017, **56**, 12155–12159.
- 26 (a) M. Auria, *Molecules*, 2014, **19**, 20482; (b) H. Ghalla, N. Issaoui, M. Govindarajan, H. T. Flakus, M. H. Jamroz and B. Oujia, *J. Mol. Struct.*, 2014, **1059**, 132–143.
- 27 (a) J. J. McKinnon, D. Jayatilaka and M. A. Spackman, *Chem. Commun.*, 2007, 3814–3816, DOI: 10.1039/B704980C; (b) M. A. Spackman, J. J. McKinnon and D. Jayatilaka, *CrystEngComm*, 2008, **10**, 377–388; (c) J. J. McKinnon, M. A. Spackman and A. S. Mitchell, *Acta Crystallogr., Sect. B: Struct. Sci.*, 2004, **60**, 627–668.
- 28 (a) C. Balachandran, N. Emi, Y. Arun, Y. Yamamoto, B. Ahilan, B. Sangeetha, V. Duraipandiyam, Y. Inaguma, A. Okamoto, S. Ignacimuthu, N. A. Al-Dhabi and P. T. Perumal, *Chem.-Biol. Interact.*, 2015, **242**, 81–90; (b) W. Wang, P. He, Y. Liang, Y. Chen, A. Xia and Q. Zeng, *ECS Trans.*, 2019, **28**, 79–89; (c) C. V. Rao, D. Desai, B. Kaul, S. Amin and B. S. Reddy, *Chem.-Biol. Interact.*, 1992, **84**, 277–290.
- 29 (a) H. Lim, B. K. Park, S. Y. Shin, Y. S. Kwon and H. P. Kim, *Arch. Pharmacol. Res.*, 2017, **40**, 524–535; (b) K.-M. Shin, I.-T. Kim, Y.-M. Park, J. Ha, J.-W. Choi, H.-J. Park, Y. S. Lee and K.-T. Lee, *Biochem. Pharmacol.*, 2004, **68**, 2327–2336; (c) F. M. da Cunha, D. Duma, J. Assreuy, F. C. Buzzi, R. Niero, M. M. Campos and J. B. Calixto, *Free Radical Res.*, 2004, **38**, 1241–1253.
- 30 (a) K. Randazzo, Z. Wang, Z. D. Wang, J. Butz and Q. R. Chu, *ACS Sustainable Chem. Eng.*, 2016, **4**, 5053–5059; (b) Z. Wang, B. Miller, M. Mabin, R. Shahni, Z. D. Wang, A. Ugrinov and Q. R. Chu, *Sci. Rep.*, 2017, **7**, 13704.
- 31 (a) M. Valko, D. Leibfritz, J. Moncol, M. T. D. Cronin, M. Mazur and J. Telser, *Int. J. Biochem. Cell Biol.*, 2007, **39**, 44–84; (b) V. Lobo, A. Patil, A. Phatak and N. Chandra, *Pharmacogn. Rev.*, 2010, **4**, 118–126.
- 32 (a) S. Son and B. A. Lewis, *J. Agric. Food Chem.*, 2002, **50**, 468–472; (b) A. H. Rosendahl, C. M. Perks, L. Zeng, A. Markkula, M. Simonsson, C. Rose, C. Ingvar, J. M. Holly and H. Jernstrom, *Clin. Cancer Res.*, 2015, **21**, 1877–1887; (c) N. Rajendra Prasad, A. Karthikeyan, S. Karthikeyan and B. V. Reddy, *Mol. Cell. Biochem.*, 2011, **349**, 11–19.
- 33 (a) Y. Zou, Y. Lu and D. Wei, *J. Agric. Food Chem.*, 2004, **52**, 5032–5039; (b) İ. Gülçin, *Toxicology*, 2006, **217**, 213–220.

- 34 (a) M. Furuhashi and G. S. Hotamisligil, *Nat. Rev. Drug Discovery*, 2008, **7**, 489–503; (b) J. Storch and A. E. Thumser, *J. Biol. Chem.*, 2010, **285**, 32679–32683; (c) M. Amiri, S. Yousefnia, F. Seyed Forootan, M. Peymani, K. Ghaedi and M. H. Nasr Esfahani, *Gene*, 2018, **676**, 171–183.
- 35 (a) A. A. Naeem, S. A. Abdulsamad, P. S. Rudland, M. I. Malki and Y. Ke, *Precis. Clin. Med.*, 2019, **2**, 192–196; (b) Z. Bao, M. Malki, S. Forootan, J. Adamson, F. Seyed Forootan, D. Chen, C. Foster, P. Rudland and Y. Ke, *Genes Cancer*, 2013, **4**, 297–314.
- 36 (a) A. Naeem, S. Abdulsamad, P. Rudland, M. Malki and Y. Ke, *Precis. Clin. Med.*, 2019, **2**, 192–196; (b) W. Al-Jameel, X. Gou, X. Jin, J. Zhang, Q. Wei, J. Ai, H. Li, A. Al-Bayati, A. Platt-Higgins, A. Pettitt, P. S. Rudland and Y. Ke, *Genes Cancer*, 2019, **10**, 80–96; (c) S. Senga, K. Kawaguchi, N. Kobayashi, A. Ando and H. Fujii, *Oncotarget*, 2018, **9**, 31753–31770.
- 37 (a) Y. Kagawa, B. A. Umaru, I. Ariful, S. K. Shil, H. Miyazaki, Y. Yamamoto, M. Ogata and Y. Owada, *Adv. Biol. Regul.*, 2019, **71**, 206–218; (b) A. Cordero, D. Kanojia, J. Miska, W. K. Panek, A. Xiao, Y. Han, N. Bonamici, W. Zhou, T. Xiao, M. Wu, A. U. Ahmed and M. S. Lesniak, *Oncogene*, 2019, **38**, 6445–6460; (c) Y. Goto, Y. Matsuzaki, S. Kurihara, A. Shimizu, T. Okada, K. Yamamoto, H. Murata, M. Takata, H. Aburatani, D. S. B. Hoon, T. Saida and Y. Kawakami, *Cancer Res.*, 2006, **66**, 4443–4449.
- 38 O. Trott and A. J. Olson, *J. Comput. Chem.*, 2010, **31**, 455–461.
- 39 E. F. Pettersen, T. D. Goddard, C. C. Huang, G. S. Couch, D. M. Greenblatt, E. C. Meng and T. E. Ferrin, *J. Comput. Chem.*, 2004, **25**, 1605–1612.
- 40 M. Turner, J. McKinnon, S. Wolff, D. Grimwood, P. Spackman, D. Jayatilaka and M. Spackman, *CrystalExplorer17*, The University of Western Australia, 2017.